X-ray reciprocal space imaging of a screw-dislocation network at a low-angle twist boundary in a $SrTiO_3$ membrane transfer-bonded to bulk $SrTiO_3$

Jeremy Maltitz,[1] Martin Schmidbauer,[1] Carsten Richter,[1] Michael Hanke,[2] Ferris Stümpel,[1] Thomas Schroeder,[1,3] Jutta Schwarzkopf,[1] and Jens Martin[1,*]

[1]*Leibniz-Institut für Kristallzüchtung, Max-Born-Str. 2, 12489 Berlin, Germany*

[2]*Paul-Drude-Institut für Festkörperelektronik, Leibniz-Institut im Forschungsverbund Berlin e.V., Hausvogteiplatz 5-7, 10117 Berlin, Germany*

[3]*Humboldt-Universität zu Berlin, Institut für Physik, Newtonstr. 15, 12489 Berlin, Germany*

(Received 20 February 2026; revised 8 May 2026; accepted 15 May 2026; published 17 June 2026)

The transfer of oxide membranes provides a new dimension in material design that goes beyond the limitations of classical hetero-epitaxy. For example, the transfer of freestanding membranes offers the in-plane twist angle between film and substrate as a tuneable degree of freedom. An ideal twist boundary yields formation of an in-plane screw-dislocation network to reduce interfacial stress. Previously, periodic screw-dislocation networks have been demonstrated by wafer bonding of two crystals, where the twist boundary is embedded in the bulk and made accessible to detailed characterization mostly by destructive methods. Recent approaches exploited freestanding membranes to create twist boundaries with the interface located only nanometers beneath the surface, making it readily accessible by near-surface-sensitive techniques. In this work, both approaches were combined to transfer membranes on the mm²-scale via wafer bonding and subsequent release by etching the sacrificial layer. High-resolution synchrotron-based grazing incidence x-ray diffraction was performed to investigate the structure of the twisted $SrTiO_3/SrTiO_3$ interface. In order to gain a better qualitative and quantitative understanding of the experimental results, we simulated the x-ray diffraction of twisted perovskites based on continuum elastic theory and kinematical scattering. Our measurements show that the measured diffraction patterns are consistent with the formation of a periodic screw-dislocation network, since the apparent superlattice reflections coincide with the obtained diffraction pattern from simulations. However, the intensity profile and appearance of specific symmetry-forbidden diffraction peaks in the experiments cannot be described by elastic displacements alone.

DOI: 10.1103/z4d4-1lj3

I. INTRODUCTION

The ability to engineer interfaces with atomic precision via hetero-epitaxy has enabled a wide range of functionalities in complex oxides, including electronic [1], structural [2], and ferroelectric phenomena [3]. Yet, the traditional hetero-epitaxial growth method has limitations, specifically, lattice matching and substrate clamping impose constraints on accessible strain states and heterostructures.

The fabrication of freestanding oxide membranes has opened a pathway to material design and interfaces that are not accessible by conventional hetero-epitaxial methods, where the functional layer is rigidly clamped to the growth substrate. Recent advances in freestanding oxides have enabled the transfer [4], controlled straining [5], and twisting [6–11], providing unprecedented degrees of freedom in oxide engineering. Especially twisted interfaces, in which the absence of perfect registry between the two lattices yields moiré superlattices [6], are of high interest for engineering functional interfaces. Recently, it has been demonstrated that twisted oxide interfaces display physical properties based on polar topologies [8,9], or twist-dependent oxygen-ion diffusion coefficients [10]. At specific twist angles, a coincidence site lattice (CSL) can arise, representing a particular geometric configuration where a subset of atomic positions from both layers within a moiré cell coincide. As a result, the twist angles that form a CSL often tend to minimize interfacial strain and yield well-defined, low-energy boundary structures [12].

In general, a pure twist boundary with any nonzero twist angle is characterized by a moiré pattern producing a structural modulation whose periodicity scales continuously with the twist angle. When the twist angle becomes sufficiently small, in turn, the moiré periodicity becomes much larger than the unit cell of the underlying crystal structure. In this limit, the minimization of the interface energy leads to the formation of screw-dislocation networks [13]. Indeed, recent sacrificial layer-based assembly approaches demonstrated that twisted membranes can generate periodic dislocation arrays in oxide perovskites [10,11].

While the formation of screw-dislocation networks is well known from wafer-bonded bicrystals [14,15] or thin metal

*Contact author: jens.martin@ikz-berlin.de

Published by the American Physical Society under the terms of the Creative Commons Attribution 4.0 International license. Further distribution of this work must maintain attribution to the author(s) and the published article's title, journal citation, and DOI.

foils [16], the twisted interfaces are generally buried deep within the bulk and therefore difficult to access experimentally [17]. In contrast, twisted interfaces formed from nanometer-thin membranes are located only a few nanometers below the surface, making them readily accessible to near-surface-sensitive characterization techniques. The surface in the vicinity of the dislocation network can also be exploited for decoration effects, enabling the formation of self-assembled nanostructures, an opportunity that is difficult to achieve with wafer bonding because of the limited accessibility of the reconstructed interface [17,18]. This opportunity is readily accessible by recent advances in oxide membrane fabrication, which allow nanometer-thick freestanding oxide membranes to be obtained by employing a sacrificial layer between the functional layer and the growth substrate [4]. This could open new avenues for controlling ionic conductivity by using the high density of strain-induced defects at grain boundaries, a key factor in technologies such as fuel cells, batteries, and catalysis [19].

A particularly interesting family of sacrificial layers are water-soluble $(Ca, Sr)_3Al_2O_6$ compounds because of their close reproduction of the perovskite lattice and their lattice parameter a between 15.263 to 15.842 Å [20], for the pure Ca and Sr compounds, respectively. One unit cell of $(Ca, Sr)_3Al_2O_6$ roughly matches the lattice of four unit cells with the pseudocubic lattice parameter ($a_{pc} = a/4$) ranging from 3.816 to 3.961 Å. Therefore, these $(Ca, Sr)_3Al_2O_6$ compounds can be epitaxially combined with a variety of common perovskite oxides, such as $SrTiO_3$ [4], $SrRuO_3$ [21], and $BaTiO_3$ [9]. As a result, $(Ca, Sr)_3Al_2O_6$ sacrificial layers have become a key component in the advancement of freestanding oxide membranes because the lattice parameter can be adjusted to reduce epitaxial strain, enabling the transfer of large-area crack-free oxide membranes [22].

In this work, we combined both wafer bonding and sacrificial layers to fabricate $SrTiO_3/SrTiO_3$ twisted interfaces with well-defined rotation angles while maintaining large-area crack-free membranes, hereafter referred to as transfer-bonding [11]. We used grazing-incidence in-plane x-ray diffraction (GIXD) for reciprocal space imaging. We probed a low-angle twist boundary of $SrTiO_3$ on a mm²-scale to investigate the moiré superlattices by detailed analysis of the position and amplitude of the superlattice reflections. To compare and assess the experimental features, the diffraction pattern of the perovskite twist boundary is simulated in the framework of kinematical scattering theory using the displacement field obtained from continuum elastic theory. This approach enables a direct link between the real-space relaxation and the observed diffraction pattern.

The manuscript is organized as follows. First, we provide the relevant experimental details of sample preparation and measurement set-up. Then, we describe the theoretically expected screw-dislocation network at an ideal twist boundary and its associated displacement field and introduce our numerical approach to simulate diffraction patterns. Finally, we present data obtained from grazing-incidence x-ray diffraction experiments and provide a detailed discussion and comparison between simulated and measured diffraction patterns, followed by conclusions.

II. EXPERIMENTAL DETAILS

$SrTiO_3$ films with thicknesses in the range 4–20 nm were epitaxially grown on a water-soluble $(Ca, Sr)_3Al_2O_6$ sacrificial layer with a thickness of 12 nm. This heterostack was grown by pulsed-laser deposition (PLD) using a KrF excimer laser ($\lambda = 248$ nm) on a (001)-oriented $SrTiO_3$ substrate with a surface miscut of 0.1°. Both $SrTiO_3$ and $(Ca, Sr)_3Al_2O_6$ films have been deposited with a substrate-to-target distance of 50 mm at a substrate temperature of 750°C and 0.1 mbar O_2 partial pressure, with a laser fluence of 1.4 J/cm² and repetition rate of 2 Hz. The target of the sacrificial layer has a nominal composition of $Ca_{1.2}Sr_{1.8}Al_2O_6$ and was prepared using a solid-state sintering procedure [4], while the stoichiometric $SrTiO_3$ target was provided by Pi-Kem Ltd. (UK). The $SrTiO_3$ substrates have been prepared according to Ref. [23] to provide a TiO_2-surface termination for both thin film epitaxy and transfer bonding. To achieve a $SrTiO_3/SrTiO_3$ twist boundary, a thin $SrTiO_3$ membrane (m-$SrTiO_3$) was transferred via transfer-bonding as described previously [11]. In brief, a clamping mechanism is manually assembled to bond the PLD-grown heterostack to a $SrTiO_3$ bonding substrate with an estimated force of 10–20 N corresponding to a pressure of about 1–2 MPa over the sample area. The clamping arrangement is placed inside a muffle furnace under ambient atmosphere and heated to 1000 °C for 1 h with a rate of 200 K/h. Subsequently, the wafer-bonded structure was placed in a tempered deionized water bath for approximately 12 h at 60 °C to dissolve the sacrificial layer. Afterwards, the nanometer-thin membrane remains attached to the $SrTiO_3$ bonding substrate with a twist angle θ.

Grazing-incidence in-plane x-ray diffraction experiments were performed at the PETRA III P08 beamline (DESY, Germany) using an x-ray energy of 11 keV ($\lambda = 1.127$ Å). Azimuthal φ scans of the sample were performed using a Dectris Eiger2 1M area detector (pixel size 75×75 μm²), providing three-dimensional intensity distributions in reciprocal space [24]. The glancing angle of incidence was set close to the critical angle of total external reflection of $SrTiO_3$ to reduce the penetration depth of the x rays (10–50 nm [25]) and thus suppress the strong scattering signal originating from the $SrTiO_3$ substrate. Supplementary experiments were performed in the homelab using a 9-kW SmartLab system (Rigaku, Japan), albeit with reduced counting statistics and angular resolution.

III. THEORETICAL MODELING

A schematic illustration of the sample with twist angle θ is shown in Fig. 1(a). At the twist boundary between the membrane and the $SrTiO_3$ substrate, a two-dimensional (2D) moiré pattern with a lateral periodicity $L = a/[2\sin(\theta/2)]$ (where $a = 3.9053$ Å [26] is the lattice parameter of $SrTiO_3$) emerges because of the superimposed crystal lattices [Fig. 1(b)]. The moiré pattern is characterized by a periodically recurring atomic arrangement as shown in Fig. 1(c). For clarity, the lattices are shown directly below and above the twist boundary along the x direction, and the axes are not equally spaced because for small twist angles θ the moiré periodicity L becomes significantly larger than the lattice parameter a.

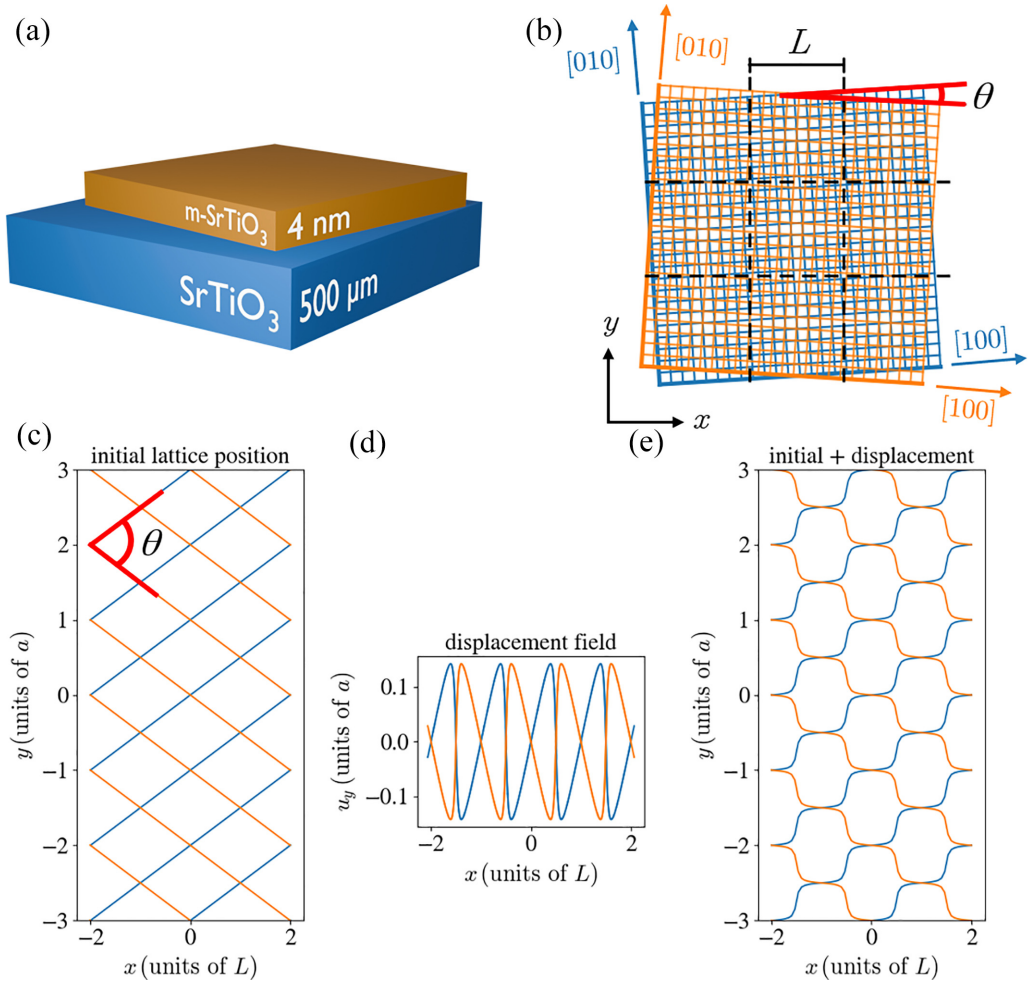


FIG. 1. (a) Schematic illustration of the transferred membrane (m-$SrTiO_3$, orange) on a $SrTiO_3$ substrate (blue). (b) Superimposed lattices from the twist boundary with twist angle θ forming a moiré pattern with periodicity L. (c) Schematic drawing of the lattices at the twist boundary along the respective [100] direction. Along [010] an orthogonal lattice would be present with the same period; this is not shown for clarity. (d) The magnitude of displacement field component u_y as a function of the x position, which acts at the twist boundary to achieve the coherent moiré cells. (e) Positions after the displacement field u_y is applied to the initial positions, i.e., the relaxed structure. Note that the scale in the y directions is a few unit cells with spacing a, while the x scale spans multiple moiré periodicities, and for small twist angles θ the moiré periodicity L is significantly larger than the lattice parameter a.

For each moiré cell, only the central atomic positions of the lower layer remain nearly overlapping with the corresponding atomic positions of the upper layer, i.e., where the lines cross. For the majority of interlayer bonding partners, the bond length is significantly increased relative to the bulk, resulting in an energetically less favorable arrangement. By introducing shear displacements in opposite directions as shown in Fig. 1(d) for the upper and lower layers, a coherent (basically unrotated) interface within each moiré cell can be recovered; see Fig. 1(e). The relaxed interface structure can be described as a screw-dislocation network [27,28]. Note that between neighboring moiré cells, atomic rows are shifted half a unit cell, because of the screw-dislocation network, which has consequences for GIXD, as discussed below.

The theoretical description of the screw-dislocation network and associated displacement field involved in going from the initial state to the relaxed state has already been given by van der Merwe in Ref. [27] within the framework of linear continuum elastic theory and is only briefly summarized here. In this model, the displacement field $\boldsymbol{u} = (u_x, u_y, u_z)$, i.e., the deviation from the initial lattice, arises from the relaxation at the interface induced by the increased bond lengths of atoms between the membrane and the substrate, resulting in a long-range 2D periodic superstructure. The displacement field is periodic with a period L corresponding to the lateral moiré periodicity. For the displacement field in the x and y directions, the underlying trigonometric form $\arctan[\sin(x)/(1+\cos(x))]$ produces the sawtooth-like displacement profile with periodicity L shown in Fig. 1(d). Additionally, the z component is equal to zero, since the screw dislocations are considered to be a pure lateral superstructure. Therefore, the following applies for the three components of the displacement field [27]:

$$u_x = \pm\frac{b}{2\pi}\arctan\left(\frac{Ae^{\mp kz}\sin(ky)}{1+Ae^{\mp kz}\cos(ky)}\right), \tag{1a}$$

$$u_y = \mp\frac{b}{2\pi}\arctan\left(\frac{Ae^{\mp kz}\sin(kx)}{1+Ae^{\mp kz}\cos(kx)}\right), \tag{1b}$$

$$u_z = 0 \tag{1c}$$

with

$$b = \frac{a}{\cos\left(\frac{\theta}{2}\right)}, \quad L = \frac{a/2}{\sin(\theta/2)}, \quad k = \frac{2\pi}{L},$$

$$\beta = 2\pi\left(\frac{\mu}{\mu_0}\right)\frac{\tan(\frac{\theta}{2})}{\cos(\frac{\theta}{2})}, \quad A = \sqrt{1+\beta^2}-\beta,$$

(x, y, z) denote the Cartesian coordinates, where the x and y axes are parallel to the boundary plane, and the z axis is the twist axis with $z = 0$ corresponding to the boundary plane. The sign $\pm$ governs the antisymmetric relations of displacement in $+z$ (above the interface) and $-z$ (below the interface), respectively. The bulk lattice parameter of $SrTiO_3$ is denoted by a, while θ represents the twist angle between the two bonded $SrTiO_3$ crystals and b corresponds to the Burgers vector of the screw dislocation. The parameter β is a measure of the strength of the displacement field and is proportional to the ratio of the interfacial and bulk shear moduli (μ/μ_0). A is a dimensionless parameter that controls the amplitude of the displacement field. For horizontal crystal planes that are increasingly distant from the twisted interface, the strength of the displacement field converges towards null, which is expressed by the exponential term $e^{\mp kz}$. Consequently, the lattices gradually approach the rotated bulk configuration depending on the distance z from the interface.

The positional changes arising from the screw-dislocation network can be incorporated within the framework of kinematical scattering theory, where the diffracted wave amplitude $A(\boldsymbol{Q})$ at a scattering vector $\boldsymbol{Q}$ is proportional to the Fourier transform of the spatially varying atomic positions modulated by the displacement field [28]. The atomic position $\boldsymbol{r}_j$ is divided into a Bravais lattice vector $\boldsymbol{r}_{N0}$ and a basis vector $\boldsymbol{b}_l$ inside the unit cell. Further, we define a structure factor for the unit cell $F(\boldsymbol{Q})$, assuming that the inhomogeneous displacement field has negligible influence on the structure factor,

$$A(\boldsymbol{Q}) = \sum_{j=1}^{n} f_j(\boldsymbol{Q})e^{i\boldsymbol{Q}\cdot\boldsymbol{r}_j} \tag{2}$$

$$= F(\boldsymbol{Q})\sum_{\boldsymbol{r}_{N0}} e^{i\boldsymbol{Q}\cdot[\boldsymbol{r}_{N0}+\boldsymbol{u}(\boldsymbol{r}_{N0})]} \tag{3}$$

with

$$\boldsymbol{r}_j = [\boldsymbol{r}_{N0} + \boldsymbol{u}(\boldsymbol{r}_{N0})] + \boldsymbol{b}_l$$

$$F(\boldsymbol{Q}) = \sum_l f_l(\boldsymbol{Q})e^{i\boldsymbol{Q}\cdot\boldsymbol{b}_l},$$

where n and m are the total numbers of atoms and unit cells, respectively, over which the amplitude is summed, with $f_j(\boldsymbol{Q})$ representing the atomic scattering factor. $\boldsymbol{b}_l$ labels the position of the lth atom within the unit cell, $\boldsymbol{r}_{N0}$ denotes the initial position of the unit cell, and $\boldsymbol{u}(\boldsymbol{r}_{N0})$ is the associated displacement field.

To avoid artificial truncation effects at the simulation boundaries, which would otherwise be present in reciprocal space, a Gaussian envelope function was applied to the scattering amplitude along the lateral x and y directions. The Gaussian standard deviation σ that takes account of the limited coherence lengths of the diffraction experiment, was adjusted such that the envelope decays to 10^{-5} of its maximum value at the edges of the simulated crystal $r_{\max}$, ensuring a smooth intensity decay. This implies for the amplitude

$$A(\boldsymbol{Q}) = F(\boldsymbol{Q})\sum_{\boldsymbol{r}_{N0}} e^{i\boldsymbol{Q}[\boldsymbol{r}_{N0}+\boldsymbol{u}(\boldsymbol{r}_{N0})]}e^{\frac{-r_{N0}^2}{2\sigma^2}} \tag{4}$$

with

$$\sigma = \frac{r_{\max}}{\sqrt{-2\log(10^{-5})}} \approx 0.2r_{\max}.$$

In kinematical scattering theory, it is often possible to factorize the diffracted wave amplitude into a product of a motif factor (in this case a single moiré cell) and a lattice factor (the periodic arrangement of moiré cells). In the case of screw-dislocation networks, however, this factorization is not possible because of the incommensurability between the moiré cell and the rotated regions far from the interface. Formally, to apply the lattice-motif factorization to any lattice vector $\boldsymbol{r}_j$, the rotated lattice vector $R_\theta\boldsymbol{r}_j$ (R_θ is the rotation matrix) would need to align with another lattice vector after a moiré vector $\boldsymbol{L}_{\text{moiré}}$, i.e., a translation of a rotated vector by one moiré lattice $R_\theta\boldsymbol{r}_j + \boldsymbol{L}_{\text{moiré}}$ must reproduce the respective rotated configuration $R_\theta(\boldsymbol{r}_j + \boldsymbol{L}_{\text{moiré}})$ up to a lattice vector $\boldsymbol{r}_k$. Because of the linearity of the rotation, this requires

$$R_\theta\boldsymbol{r}_j + \boldsymbol{L}_{\text{moiré}} = R_\theta(\boldsymbol{r}_j + \boldsymbol{L}_{\text{moiré}}) + \boldsymbol{r}_k, \tag{5}$$

thus

$$\boldsymbol{L}_{\text{moiré}} = R_\theta\boldsymbol{L}_{\text{moiré}} + \boldsymbol{r}_k. \tag{6}$$

This condition is satisfied only when the twist angle is commensurate with the lattice symmetry, meaning that the rotation belongs to the discrete symmetry group of the lattice, which excludes arbitrary twist angles. Figure 9 in Appendix B shows a visual illustration of this characteristic.

Hence, this characteristic property of two crystals that are twisted relative to each other and exhibit a screw-dislocation network at the interface requires that the sum in Eq. (4) must be performed over a sufficiently large number of moiré cells, which significantly increases the computational effort. In the experiment, coherent summation is typically performed over several square micrometers, which corresponds to about one million moiré cells. In the simulations, we typically use $36 \times 36 = 1296$ moiré cells in order to keep the computational cost within reasonable limits. Details about the performed calculations are provided in Appendix A.

IV. RESULTS AND DISCUSSION

We will first examine experimental data recorded from one-dimensional (1D) azimuthal φ scans performed in GIXD geometry, which are shown in Fig. 2 for samples with different twist angles. All data display distinct membrane and substrate Bragg peaks, separated by the in-plane twist angle θ. Figure 2(a) illustrates 020 φ scans for seven samples with the SmartLab home diffractometer, whereas Fig. 2(b) displays 010 φ scans for some of these samples at the P08 beamline

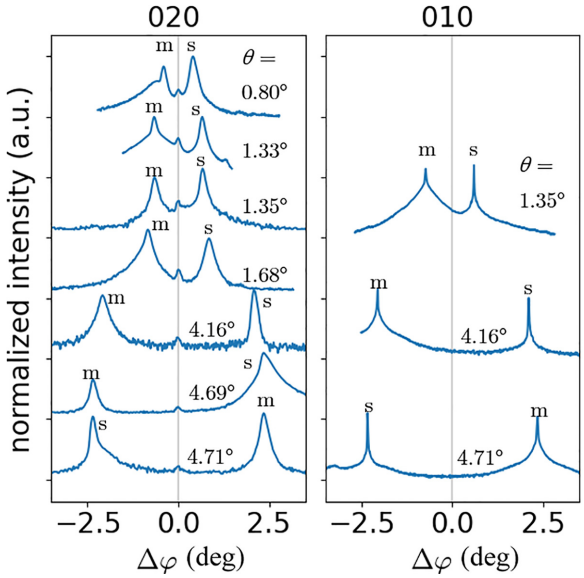


FIG. 2. Grazing-incidence azimuthal φ-scans around the (a) 020 and (b) 010 Bragg reflections of samples with different twist angles θ ranging from 0.80° to 4.71°±0.01°. All data display a distinct membrane (m) and substrate (s) reflection, separated by the in-plane twist angle θ. For some samples, the peaks are not symmetrical because of unbound membrane fragments, which can randomly orient themselves after dissolution of the sacrificial layer during the separation step. In (a), a weak peak can be identified midway between membrane and substrate, which can be assigned to the unrotated coherent interface at the twist boundary. The data are shown with a vertical offset for clarity, while relative intensities are preserved.

of the PETRA III synchrotron radiation facility. Taking into account that the total probed area in GIXD geometry is in the range of mm², the well-defined main peak of the transferred film indicates a very low mosaicity. Indeed, the peak width of the transferred film remains compatible with that of the substrate (data in Fig. 10, Appendix B). This is a result of the transfer-bonding process, which maintains the original in-plane long-range registry. For the 020 Bragg reflection, an additional peak exactly in the middle of the membrane and substrate peak can be identified. This central peak can be assigned to the unrotated coherent interface at the twist boundary. It is a direct consequence of lattice relaxation and does not appear if the transferred membrane and substrate form only a mere moiré pattern. This demonstrates that the sample fabrication method is a reliable way of bonding the membrane to the bonding substrate for arbitrary twist angles.

However, the central peak is always missing in the 010 φ scans [Fig. 2(b)]. To understand this, we have to take a closer look at the relaxed interface. Specifically, we need to inspect the atomic arrangement at neighboring moiré cells. A schematic illustration of the screw-dislocation network is shown in Fig. 3(a), where the coherent interface is formed within each moiré cell at the expense of the dislocation lines between the moiré cells indicated by the dashed lines. Figure 3(b) shows a schematic of adjacent moiré cells at the twisted interface. For simplicity, the lattices at the interface are represented by primitive cubic cells. Because of the presence of in-plane screw dislocations, the respective 2D lattice

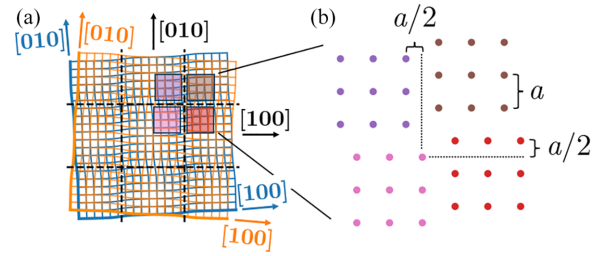


FIG. 3. (a) Illustration of the screw dislocations at the interface formed by the relaxed twist boundary. As a result of relaxation, a coherent interface is formed with a crystallographic orientation that lies exactly between the membrane and substrate orientation. (b) Simplified illustration of adjacent moiré cells comprised of unit cells with lattice parameter a to emphasize the lattice relations of the moiré cells. Because of the shifts, the crystal lattice parameter at the interface is effectively $a/2$.

is shifted by $a/2$ in the x and y directions. This shift leads to a doubling of the moiré length in real space that should be expressed as a half moiré length in reciprocal space. However, because of these relative shifts, the crystal lattice parameter at the interface is effectively $a/2$, resulting in a doubled spacing in reciprocal space. Thus, the central Bragg reflections of the relaxed interface only occur at reciprocal-lattice points where h and k are both even.We are now turning to two-dimensional in-plane intensity distributions. For the sample with a twist angle of 4.16° (see Fig. 2) the experimental diffraction patterns in the vicinity of the 020 and $\bar{1}10$ Bragg reflections are shown in Figs. 5(a) and 5(b) (see below), respectively. Both diffraction patterns show two major peaks corresponding

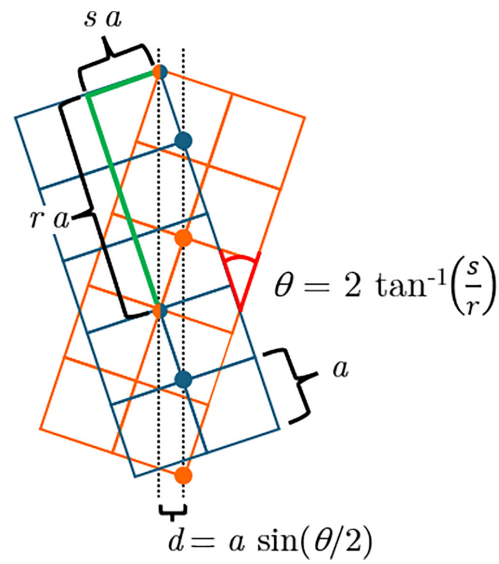


FIG. 4. Geometric construction of the coincident-site lattice formed by the rotated membrane and substrate lattices. The integers r and s define the coincidence conditions of the shared net planes, which satisfy $s/r = \tan(\theta/2)$. The resulting coincident site lattice forms vertical (and horizontal) net planes with spacing d, giving rise to shared high-order Bragg reflections at $s\,r\,0$ and $-s\,r\,0$ for the substrate and membrane, respectively. In this image, $r = 3$ and $s = 1$ were chosen as an illustrative example.

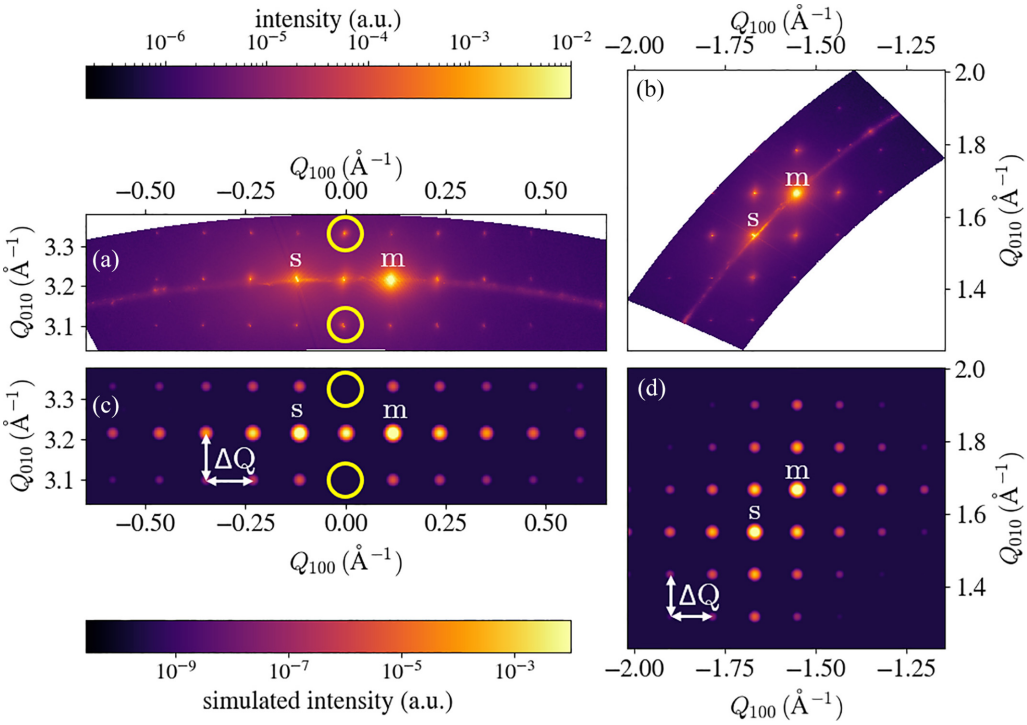


FIG. 5. Experimental grazing incidence x-ray diffraction patterns of a m-$SrTiO_3$/$SrTiO_3$ twist boundary in the vicinity of the (a) 020 and (b) $\bar{1}10$ $SrTiO_3$ in-plane Bragg reflections. The labels of the main peaks from the substrate (s) and membrane (m) reference the peaks immediately below the label, while the yellow circles indicate symmetry-forbidden peaks caused by an ideal screw-dislocation network. (c), (d) Calculations of a pure screw-dislocation network ($\theta = 4.16°$) around the 020 and $\bar{1}10$ Bragg reflections, respectively, to be compared with (a) and (b). The FWHM of the peaks is limited by the calculation size as described in Appendix A.

to the membrane (m) and substrate (s) contributions, respectively. In addition, a weak Debye-Scherrer-ring-like intensity distribution can be identified, most likely originating from scattering by small randomly oriented loose fragments of the transferred membrane, created during the separation process of the growth and bonding substrate.

Regardless of the selected Bragg reflection, the separation between the membrane and substrate peak consistently appears along the angular direction (i.e., perpendicular to the scattering vector), whereas their radial positions along the scattering vector are identical. This is a direct consequence of the twisted interface, where the membrane and the substrate lattices differ by an in-plane rotation while both share the same in-plane lattice parameter. From the measured angular separation, a twist angle of $\theta = 4.16 \pm 0.01°$ is obtained.

In addition to the membrane and substrate Bragg reflections, a square arrangement of sharp peaks aligned along Q_{100} and Q_{010} can be identified for both Bragg reflections shown in Figs. 5(a) and 5(b) (see above). The measured superlattice peak spacing $\Delta Q = (0.117 \pm 0.001)$ Å^{-1} corresponds to a real-space periodicity of $L_{\text{super}} = 2\pi/\Delta Q = (5.38 \pm 0.05)$ nm, which is in excellent agreement with the moiré periodicity $L_{\text{moiré}} = (5.37 \pm 0.01)$ nm expected from a twist angle of $\theta = (4.16 \pm 0.01)°$.

It is important to note that the observed superlattice reflections are not the signature of the real-space moiré pattern and cannot be explained by the interference of two superimposed lattices. For the case of two perfect periodic lattices twisted with respect to each other, the diffraction signal corresponds to the coherent superposition of two independent reciprocal lattices, since the scattered amplitudes of the two lattices can be added separately. In the experiment, membrane and substrate peaks are generally very sharp, with the typical peak width being much smaller than their angular separation owing to the twist angle. As a result, membrane and substrate peaks are well separated and the interference of the individual scattering amplitudes is expected to be close to the background intensity. Yet, the observed superlattice peaks reach up to four orders of magnitude higher than the corresponding background intensity.

In addition, from a geometrical perspective, peaks corresponding to "untwisted" lattice planes have to be caused by shared net planes of membrane and substrate that are aligned vertically, as shown in Fig. 4. Such shared net planes, i.e., the coincidence-site lattices, exist under the following condition [29]:

$$\frac{s}{r} = \tan\left(\frac{\theta}{2}\right) \tag{7}$$

with s and r being the integers defined in Fig. 4. However, especially for small twist angles these integers can become very large. Moreover, these shared net planes exhibit a very small net plane distance of about $d = a\sin(\theta/2)$. When displaying all such vertical (or horizontal) net planes, they are equally spaced, forming a regular "sublattice". As indicated by Fig. 4, the high-order Bragg peaks with an expected peak midway between membrane and substrate are ($s\,r\,0$). In particular, a twist angle θ of 4.16° (from the experiment) corresponds to approximately $s/r = 1/28$. Therefore, the shared high-order Bragg peaks of substrate and rotated membrane appear at very

large scattering vectors at the 1 28 0 and $\bar{1}$ 28 0 reflections, respectively, far away from the membrane and substrate reflections under investigation.

To confirm this, we have performed calculations of the diffraction of two rotated cubic lattices with similar dimensions and a 4.16° twist angle in Figs. 5(c) and 5(d) in the vicinity of the 020 and 0 28 0 Bragg reflections. In Fig. 11 in Appendix B, calculations for a purely twisted lattice without inclusion of any displacement field, which show no indication of superlattice reflections. This demonstrates that a simple superposition of two rigid lattices, and the associated interference effects, are insufficient to produce the observed superlattice peaks. These results are consistent with recent experiments and numerical simulations on twisted bilayer graphene [30] or buried moiré supercells [31]. Also in these cases, superlattice diffraction peaks in the vicinity of the main peaks appear only in the presence of lattice distortions within the structures. Therefore, the appearance of a superlattice pattern is an unambiguous indication of lattice relaxation at the interface with the same two-dimensional periodicity as the moiré pattern. These results are consistent with the formation of a periodic array of screw dislocations as expected from an ideal twist grain boundary [14,16].

To gain more detailed structural information about the observed superlattice, we have simulated 2D GIXD patterns within the framework of kinematical scattering theory, combined with linear continuum elastic theory to calculate the strain field of a dislocation network as described above in Sec. III. Figures 5(c) and 5(d) show the simulated diffraction patterns of the 020 and $\bar{1}$10 Bragg reflections, which can be compared to the corresponding experimental data shown in Figs. 5(a) and 5(b), respectively.

Very good agreement between the simulated and experimental diffraction patterns could be achieved. This concerns, on the one hand, the presence and positions of the fundamental Bragg peaks of the substrate (s) and membrane (m). In addition, the simulation reproduces the two-dimensional superlattice pattern observed in the experiment, which is obviously caused by the periodic screw-dislocation network. However, please note that the full width at half maximum (FWHM) of all peaks in the simulations is consistently too large (for line sections, see Fig. 12 in Appendix B). This is caused by the limited number of moiré cells used in the simulations, which is 36×36 in our case. A more detailed explanation is given in Appendix A.

Let us take a closer look at the superlattice diffraction pattern in the vicinity of the experimental 020 Bragg reflection shown in Fig. 5(a). The square two-dimensional arrangement of the superlattice peaks is a consequence of the periodic strain field caused by the two-dimensional arrangement of screw dislocations at the twist boundary [11]. In particular, superlattice peaks aligned along Q_{010} are caused by the periodic arrangement of screw dislocations along the respective crystallographic direction [010], whereas superlattice peaks aligned along Q_{100} are caused by the periodic arrangement of screw dislocations along [100]. For the first case, the scattering vector $\boldsymbol{Q}$ is perpendicular to the Burgers vectors $\boldsymbol{b}_\perp$, as shown in Fig. 6, where $\boldsymbol{k}_0$ represents the incident wave vector and $\boldsymbol{k}$ the diffracted wave vector. The condition $\boldsymbol{b}_\perp \cdot \boldsymbol{Q} = 0$

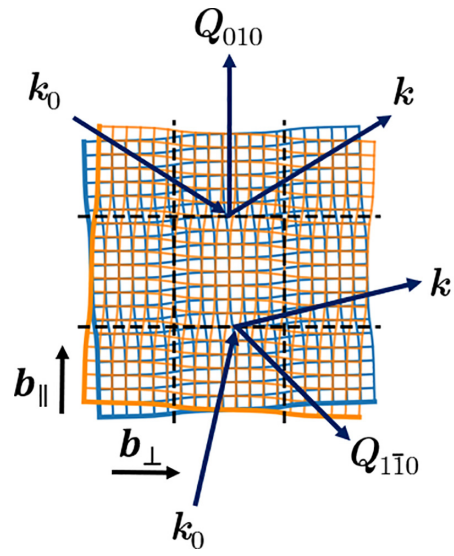


FIG. 6. Schematic illustration of the diffraction geometry, where $\boldsymbol{k}_0$ represents the incident wave vector, $\boldsymbol{k}$ the diffracted wave vector, and $\boldsymbol{Q}$ the scattering vector. At this specific diffraction condition, one Burgers vector lies parallel $\boldsymbol{b}_\parallel$ and the other perpendicular $\boldsymbol{b}_\perp$ to the scattering vector. For clarity, the scattering vector $\boldsymbol{Q}_{1\bar{1}0}$ is shown, which is symmetry equivalent to $\boldsymbol{Q}_{\bar{1}10}$.

is known as the invisibility criterion, and consequently, this leads to a vanishing diffracted intensity of the superlattice peaks at $Q_{100} = 0$; see Fig. 5(c). On the other hand, for the second case of screw dislocations that are periodically aligned along [100], the corresponding Burgers vectors $\boldsymbol{b}_\parallel$ are collinear with the scattering vector $\boldsymbol{Q}$. Therefore, in the vicinity of the central peak at $Q_{010} = 3.21$ Å^{-1} , the superlattice peaks aligned along Q_{100} do not vanish.

The invisibility criterion is no longer strictly valid when the diffraction vector contains both h and k components. In this case, the scattering vector $\boldsymbol{Q}$ has a projection along both in-plane directions, such that both sets of Burgers vector have components parallel to $\boldsymbol{Q}$. Consequently, diffraction vectors with nonzero h and k indices probe both sets of dislocations simultaneously, lifting the invisibility criterion observed for pure [100] and [010] directions, as seen in Figs. 5(b) and 5(d).

Additional insight can be gained by comparing the measured and calculated intensities. Figure 7(a) shows line scans of the experiment from Fig. 5(a) taken at $Q_{010} = 3.21$ Å^{-1} parallel to Q_{100}. The contrast between the intensities observed experimentally and the intensities achieved numerically is plotted in Fig. 7(b). The numerical results are obtained from a supercell of lateral size of 500 crystal unit cells, which corresponds to 36 moiré cells - with a total thickness of about 10 nm (or 25 unit cells) in the z directions to roughly match the intensity ratio of the membrane peak (m) and the substrate peak (s). Within the continuum elastic theory for ideal screw dislocations [27], the intensity distribution of the superlattice peaks is a function of the parameter β [Eq. (1)], which determines the amplitude of the displacement field through the ratio of the shear moduli μ/μ_0 of the interface and the

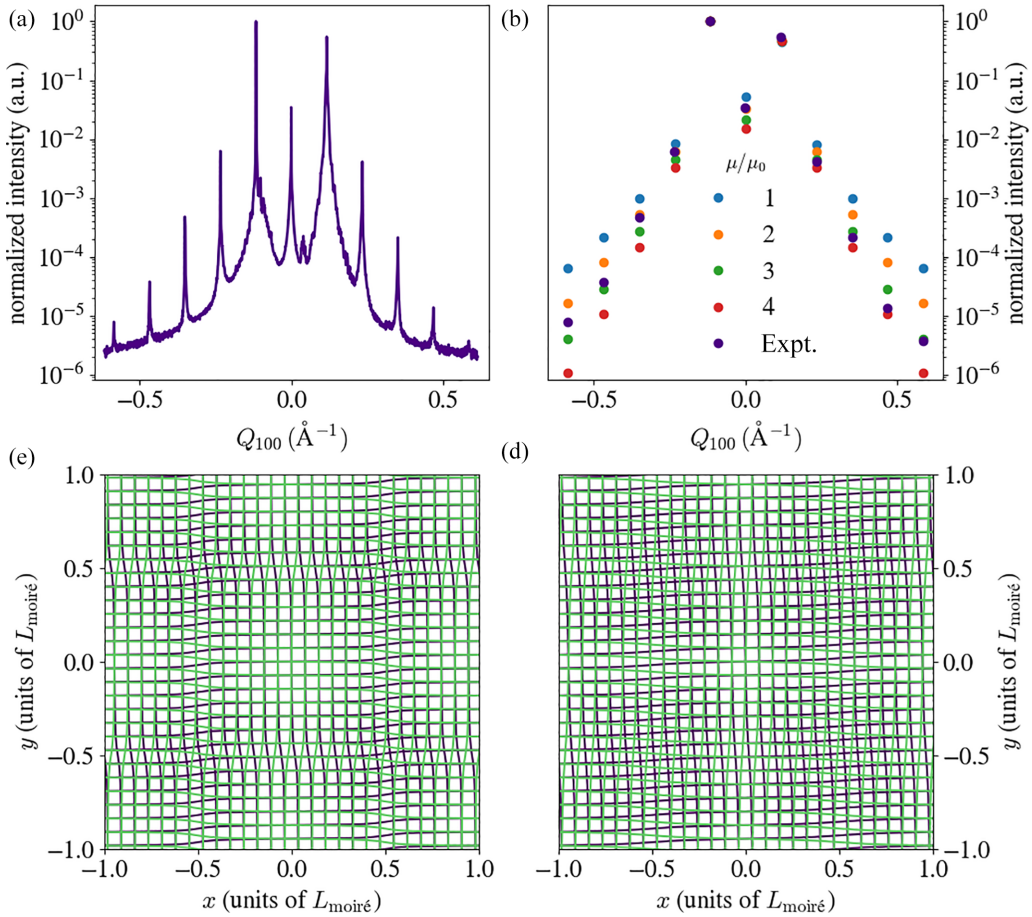


FIG. 7. (a) Line sections taken from the experimental 020 Bragg reflections shown in Fig. 5(c) along $Q_{010} = 3.21$ Å^{-1} . The numbers indicate the order of the superlattice peaks, whereas 0 is the central peak between the substrate (s) and the membrane (m). (b) The superlattice peak intensities obtained by calculations performed with different μ/μ_0 ratios to illustrate the influence on the intensity decay. Panels (c) and (d) are visualizations of the screw dislocation's real-space structures in dependence of the μ/μ_0 ratios with complete ($\mu/\mu_0 = 1$) and partial ($\mu/\mu_0 = 3$) relaxation, respectively. In (d) the dislocation lines between adjacent moiré cells are less pronounced because of the partial relaxation, resulting in a smoother and wider transition area between the moiré cells.

bulk. A higher value of β corresponds to a stiffer interface, where the displacement field is rather localized near the dislocation lines. Consequently, the coherent moiré cells are less pronounced, leading to corresponding changes in the intensity distribution. From the intensity profiles plotted in Fig. 7(b), it is obvious that the experimental superlattice intensities decay more rapidly than predicted by the elastic model with a ratio of $\mu/\mu_0 = 1$.

A comparison between simulations and experiment indicates that the shear modulus at the interface is approximately 3 to 4 times larger than the shear modulus of the bulk μ_0. This suggests that the $SrTiO_3/SrTiO_3$ interface exhibits a higher shear stiffness, leading to a less pronounced displacement field and smoother transitions between adjacent moiré cells compared to an ideal screw-dislocation network. This behavior is illustrated in Fig. 7(c) for $\mu/\mu_0 = 1$ and in Fig. 7(d) for $(\mu/\mu_0) = 3$. Consequently, the edges of the moiré cells are less distorted, and the amount of coherently overlapping unit cells within the moiré cell is reduced, as shown in Fig. 7(d), where the dislocation lines are less pronounced in comparison to Fig. 7(c). However, this interpretation is based solely on continuum elastic theory and the assumption of an ideal screw-dislocation network, and an increase of the shear modulus by a factor of 3 seems unlikely. While a screw-dislocation network represents one possible mechanism of strain accommodation, it corresponds to a specific, idealized limit in which the displacement field is localized into topological defects at an interface with complete bonding. The effective parameter μ/μ_0 in the model should be understood as capturing such deviations from the idealized dislocation-network description

Further, we cannot rule out sample-specific effects, such as the possibility that the interfacial bonding is only partial, mimicking a stiffer membrane and resulting in partial relaxation. Another reason for the decreasing peak intensities could be the intrinsic surface roughness (Fig. 13 in Appendix B) of the membrane and substrate surfaces involved, which may also affect the formation of the screw-dislocation network.

Additionally, polar-vortex topologies have recently been reported in twisted $SrTiO_3$ bilayer systems and represent an additional degree of freedom that may emerge from moiré-driven reconstructions [8,32]. Such polarization textures are associated with subtle ionic displacements (<10 pm) and local symmetry breaking, which could, in principle, give rise to diffraction features that are not captured by a purely elastic

displacement model. In particular, they may contribute to intensity at symmetry-forbidden positions through modulation of the local structure factor and consequently do not obey the invisibility criterion. The experimental observation of forbidden peaks in Fig. 5(c) indicates deviations from a purely screw-type dislocation network, suggesting additional structural changes at the interface. Notably, the substrates used in this study have a nominal miscut of 0.1°, and the presence of mixed dislocations would be expected to introduce a tilt component, giving rise to a corresponding shear of the superlattice peaks in reciprocal space [14]. However, although a mixed dislocation character would be expected to induce a sheared superlattice pattern, we already estimated that the upper limit of the tilt angle is 0.05° [11]. Therefore, mixed dislocations (with nonzero tilt component of Burgers vector) would occur every few hundred nanometers, which is much larger than the moiré periodicity of 5.38 nm. Consequently, only a very small fraction of these mixed dislocations is expected, which could not give rise to the significant intensity of the symmetry-broken peaks. Further, we would like to highlight that our transfer bonding method, similar to large-scale wafer-bonding, minimizes twist angle variations and strain as is otherwise known from the transfer of freestanding membranes. We observed sharp superlattice peaks, yielding an upper limit of twist-angle variations of 0.02°; hence a significant contribution to the symmetry-broken peaks can be excluded.

Microscopy studies on low-angle twist boundaries in wafer bonded $SrTiO_3$ have revealed similar deviations from ideal screw-dislocation models. High-resolution transmission electron microscopy (TEM) images show expanded and structurally perturbed dislocation cores, while electron energy-loss spectroscopy (EELS) analysis indicates oxygen deficiency in the cores, given by an increased Ti/O ratio and reduced Ti oxidation state in the dislocation cores [33,34]. These observations suggest that the $SrTiO_3$/$SrTiO_3$ twist boundary exhibits complex atomic and electronic reconstructions beyond the scope of models based purely on displacement.

Additionally, previous work has shown that periodic atomic displacement fields can give rise to superlattice diffraction peaks. In particular, localized in-plane and out-of-plane corrugation at the interface of a lattice-relaxed $SrTiO_3$-$(La,Sr)(Al,Ta)O_3$ heterostructure were modeled with a periodicity set by the moiré lattice and analyzed via three-dimensional fast Fourier transforms. These calculations revealed pronounced superstructure scattering in the form of Bragg rods extending along the out-of-plane direction, as well as a highly ordered in-plane superlattice. Importantly, both in-plane and out-of-plane displacements produced the same superlattice periodicity, demonstrating that periodic lattice displacements alone are sufficient to generate superlattice peaks [31].

The combination of these results with the presented diffraction analysis indicates that elastic displacement fields according to ideal screw dislocations alone are not sufficient to account for the observed diffraction pattern owing to symmetry constraints. Rather, they point to an interplay between structural reconstructions in the dislocation cores and local stoichiometric variations, which modify the effective structural symmetry and lead to the emergence of additional superlattice peaks, which would otherwise be symmetry-forbidden.

V. CONCLUSIONS

In conclusion, we demonstrated an efficient transfer of oxide membranes via transfer-bonding, achieving a well-defined twist angle with minimal variation of the twist angle across the entire sample. As a result of lattice relaxation, superlattice peaks appear in reciprocal space, whose spacing reflects the real-space periodicity of an in-plane screw-dislocation network. The simulations based on continuum elastic theory and kinematical scattering qualitatively reproduce the experimentally observed lateral superlattice reflections. However, the experimental observation of symmetry-forbidden superlattice peaks indicates that the diffraction pattern cannot be fully described by a pure screw-dislocation model. Further investigations are necessary to clarify whether effects like structural changes in dislocation cores or the incommensurability of crystal and moiré lattice give rise to the appearance of the forbidden peaks. A more detailed characterization of the local atomic structure of the dislocations, for example through higher-level computational approaches or TEM, may further elucidate the microscopic origin of these effects.

ACKNOWLEDGMENTS

The authors thank Uwe Jendritzki for the design of the clamping mechanism, Manon Varenne for supporting GIXD measurements, and Florian Bertram (P08, DESY) for technical assistance. We thank Federal Ministry of Education and Research (BMBF) of Germany for funding the Eiger2 1M detector via ErUM Pro 05K19FK2 (Murphy, CAU Kiel). We acknowledge the funding from the DFG Grants “nano-twist”, No. MA 9075/1-1, No. SCHW 1500/9-1, and the European Regional Development Fund ERDF (Project No. 1.8/15).

DATA AVAILABILITY

There are no publicly available research data or software supporting this manuscript. Requests for further information or data should be sent to the authors.

APPENDIX A: THEORETICAL CALCULATIONS

For the numerical simulations of the diffraction pattern, a three-dimensional grid of $500 \times 500 \times 25$ unit cells was used to represent the crystal volume, which is equivalent to a lateral size of 36×36 moiré cells. This size is roughly 1/64 of the lateral size of approx. 4000×4000 required to simulate the correct FWHM of the experimental data. The vertical coordinate (z) ranged from –15.5 to +10.5 unit cells to reproduce the relative intensities observed experimentally between the substrate and the membrane, while the uppermost 10 unit cells are set to respect the thickness of the membrane. The interface was centered at $z = 0$, corresponding to the transition region between the two rotated lattices, with the upper and lower crystal halves initialized at $z = \pm 0.5$ lattice units.

In the framework of the kinematical approximation, the diffraction amplitude can often be separated into contributions from the underlying lattice and from the motif, assuming that both are commensurate and can therefore be factorized.

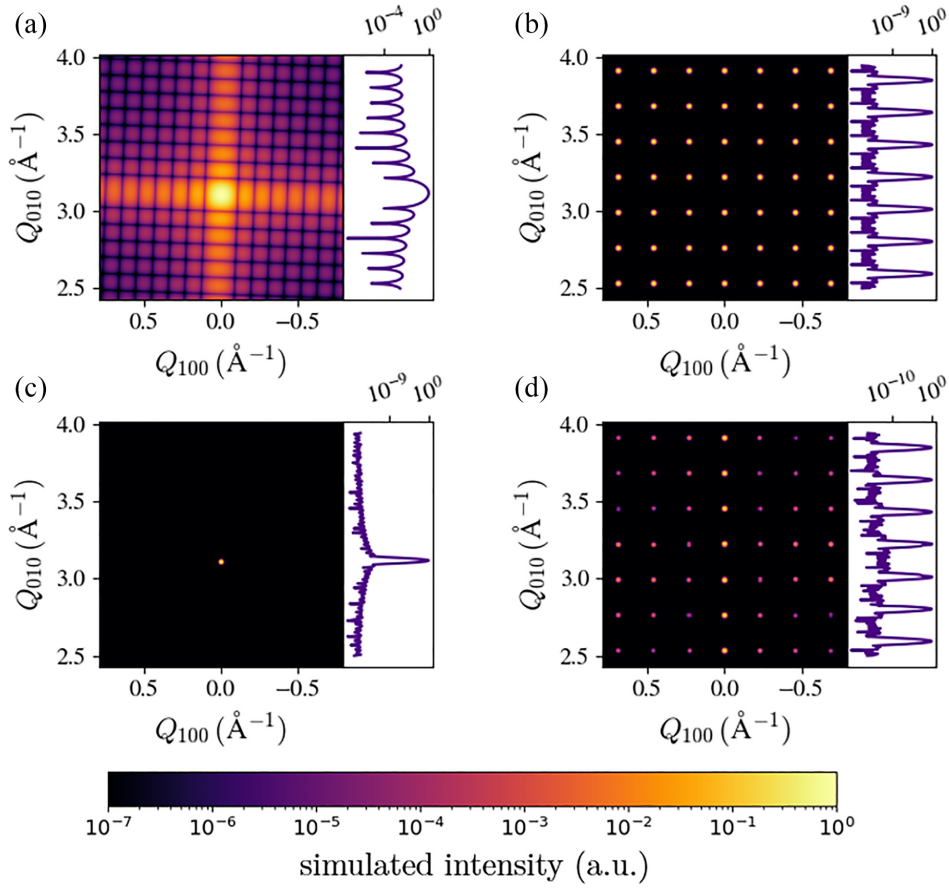


FIG. 8. (a) Scattering intensity of a 14 × 14 rotated lattice far away from the twist boundary. (b) Corresponding lattice factor for a 50 × 50 repetition of the rotated 14 × 14 motif. The lattice factor itself does not contain any information about intensity distributions, and therefore all peaks are of constant intensity. (c) Correct lattice-motif factorization when the lattice factor is rotated by the same angle as the structure factor, resulting in a single peak as expected from a single crystal. (d) Lattice-motif factorization when the lattice factor is aligned with the screw dislocations, leading to artificial superlattice peaks from the lattices far away from the interface with varying intensity distribution originating from the thickness oscillations in (a). The line scans on the right side are taken along $Q_{100} = 0$.

However, for pure twist boundaries described by screw dislocations, this separation breaks down. The relative rotation between the unaffected crystals and the interface leads to a lack of commensurability between the lattice and the motif, as represented in reciprocal space by Figs. 8(a) and 8(b), respectively. As a consequence, the motif is no longer strictly periodic with respect to a single lattice, and the conventional lattice-motif factorization cannot be applied since it results in artificial superlattice peaks, as demonstrated in Fig. 8(d). Instead, the diffraction must be treated by explicitly including the displacement field in the scattering formalism, leading to the necessity of computing larger structures, which naturally account for the incommensurate modulation introduced by the twist. In computational terms, this necessitates a more brute-force approach since a twist boundary, including the relaxed interface and the unperturbed lattices, cannot be reduced

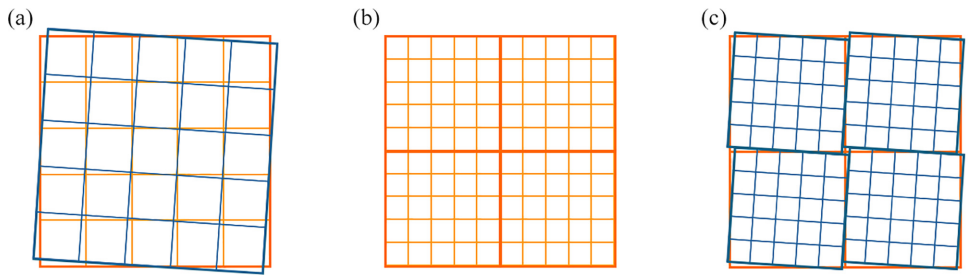


FIG. 9. (a) Schematic illustration of the rotated lattices (blue) and relaxed lattices (orange) at the interface within one moiré cell as indicated by the bold line. (b) The relaxed lattice at the interface is reproduced by translating along the [100] and [010] directions of the moiré lattice. (c) The corresponding translation of the rotated lattice is not aligned to the crystallographic directions of the moiré lattice, leading to a misalignment of the rotated lattice and therefore is not properly reproduced. The angle in this illustration is exaggerated; however, because of the geometrical mismatch, there will always be a small misalignment.

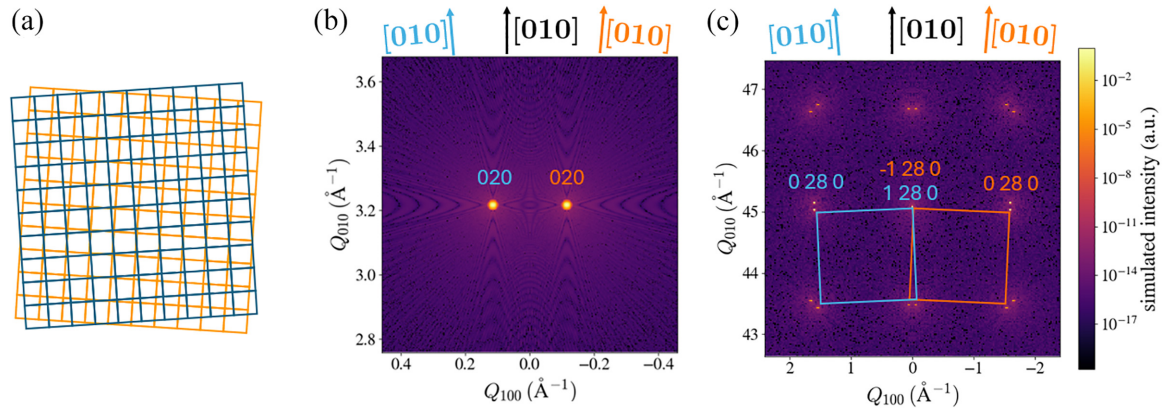


FIG. 10. (a) Sketch of two twisted lattices used for the simulated diffraction patterns shown in (b) and (c) with lateral sizes of 500 × 500 points in the vicinity of the 0 2 0 and 0 28 0 Bragg reflections, respectively. These intensities have been calculated from the ideal twisted lattices using discrete atomic positions without lattice relaxation or atomic displacements, demonstrating that diffraction from a geometrical moiré lattice does not lead to substantial interference and thus to any strong superlattice peaks as experimentally observed in Figs. 5(a) and 5(b).

to a single motif that is periodically reproduced by the lattice. Instead, the full structure must be treated explicitly over a large range of moiré cells, with the displacement field resolved at each lattice site.

Figure 9 shows a visual illustration on why the lattice factor and motif are not commensurate. In Fig. 9(a), the dashed black lines indicate the moiré cell that is to be replicated, and the orange and blue lines indicate the lattices at the interface and far away from the interface, respectively. The orange lattice coincides with the orientation of the lattice factor and can reproduce the structure shown in Fig. 9(b). The rotated lattice, however, is not aligned with the lattice factor and is not properly reproduced, as shown in Fig. 9(c).

APPENDIX B: SUPPORTING INFORMATION

Figure 10 shows simulated diffraction patterns obtained from ideal twisted lattices constructed without incorporating lattice relaxation or additional atomic displacements. The calculations are performed in the vicinity of 0 2 0 and 0 28 0 Bragg reflections to highlight that the shared lattice planes are present at high-order Bragg reflections, far away from the experimentally measured Bragg reflections. The results demonstrate that a purely geometrical moir pattern, in the absence of structural relaxation or atomic displacements, does not give rise to pronounced superlattice reflections.

Figure 11 presents an overlay of normalized diffraction peak profiles from the membrane and substrate after alignment to their respective peak centers and normalization to unit maximum intensity. This procedure removes differences in absolute intensity and enables a direct comparison of peak shapes. The analysis shows that the full width at half maximum is comparable across the majority of measured samples. A notable exception is observed for the $\theta = 4.69°$ sample, where the substrate peak exhibits additional broadening attributed to unintentional diffraction contributions originating from the edge of the substrate. This effect leads to an apparent increase in the extracted peak width but does not reflect an intrinsic change in the lattice quality.

Figure 12 displays one-dimensional line cuts through both experimental and simulated reciprocal-space maps at the 020 reflection position along $Q_{010} = 3.21$, Å^{-1}. The simulations are shown for different values of the μ/μ_0 ratio, illustrating how this parameter influences the intensity distribution

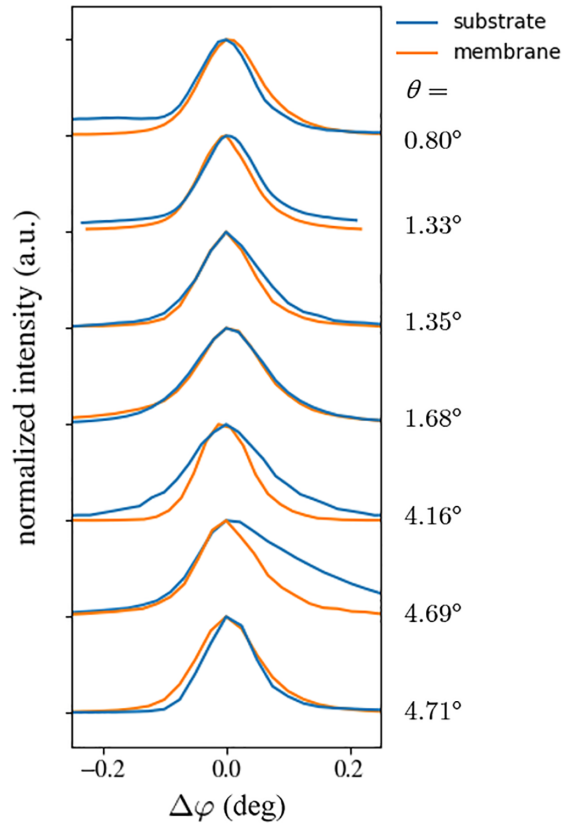


FIG. 11. Overlay of the main membrane and substrate peak after alignment to their peak centers and individual normalization to unity taken from the experimental data shown in Fig. 2. By centering each peak at zero and scaling to the same maximum intensity, differences in absolute intensity are removed, allowing a direct comparison of the peak shapes and full widths at half maximum (FWHM). The strong overlap demonstrates that the FWHM is comparable across all measurements. In the case of the $\theta = 4.69°$ sample, the substrate peak shows unintentional diffraction contributions from the edge of the substrate, artificially broadening the peak profile.

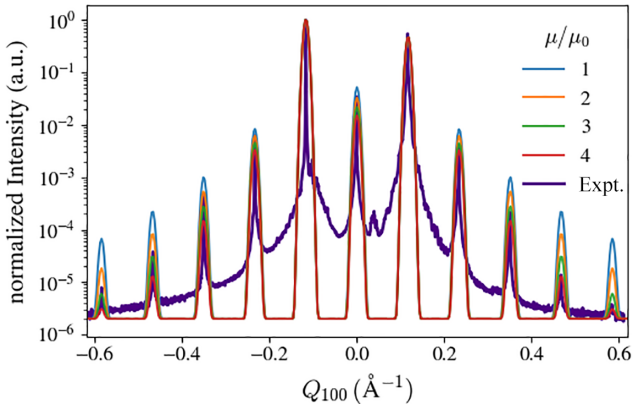


FIG. 12. Line sections from the experimental and simulated 020 reciprocal lattice points along $Q_{010} = 3.21$ Å^{-1} shown in Figs. 5(a) and 5(c). The simulations are shown with different μ/μ_0 ratios to illustrate the influence on the intensity distribution profile. The FWHM of the simulation is broader because of the limited lateral size of the calculated structure over 500 × 500 unit cells. To match the FWHM of the experiment, the simulation would require a size of 4000 × 4000 unit cells.

in reciprocal space. The broader full width at half maximum observed in the simulated data compared to experiment [Figs. 5(a) and 5(b)] is attributed to the finite lateral size of the modeled system, which is limited to 500 × 500 unit cells.

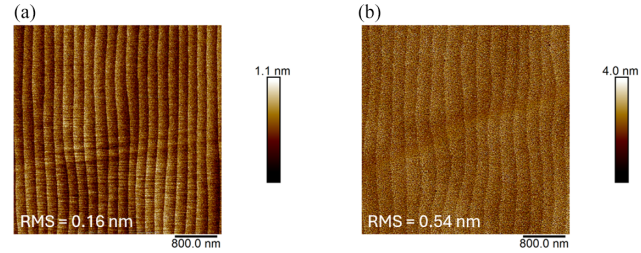


FIG. 13. AFM images of the surfaces that are involved in the bonding process. (a) Surface of the target substrate and (b) the as-grown PLD heterostack (initial top side of the membrane). The surfaces show a well-defined step-and-terrace morphology. The regular terraces separated by a one-unit-cell-high step indicate a crystalline surface with high surface quality.

Convergence tests indicate that a significantly larger lateral extent, on the order of 4000 × 4000 unit cells, is required to quantitatively reproduce the experimentally observed peak widths.

Figure 13 shows atomic force microscopy images of the two surfaces involved in the bonding process, namely the target substrate and the as-grown pulsed laser deposition heterostructure prior to transfer. Both surfaces exhibit a well-defined step-and-terrace morphology characteristic of high-quality crystalline termination. The terraces are separated by monolayer-height steps, indicating a well-ordered surface with minimal roughness on the nanoscale.

[1] A. Ohtomo and H. Y. Hwang, A high-mobility electron gas at the $LaAlO_3/SrTiO_3$ heterointerface, Nature (London) **427**, 423 (2004).

[2] S. J. May, J.-W. Kim, J. M. Rondinelli, E. Karapetrova, N. A. Spaldin, A. Bhattacharya, and P. J. Ryan, Quantifying octahedral rotations in strained perovskite oxide films, Phys. Rev. B **82**, 014110 (2010).

[3] D. G. Schlom, L.-Q. Chen, C. J. Fennie, V. Gopalan, D. A. Muller, X. Pan, R. Ramesh, and R. Uecker, Elastic strain engineering of ferroic oxides, MRS Bull. **39**, 118 (2014).

[4] D. Lu, D. J. Baek, S. S. Hong, L. F. Kourkoutis, Y. Hikita, and H. Hwang, Synthesis of freestanding single-crystal perovskite films and heterostructures by etching of sacrificial water-soluble layers, Nat. Mater. **15**, 1255 (2016).

[5] R. Xu, J. Huang, E. S. Barnard, S. S. Hong, P. Singh, E. K. Wong, T. Jansen, V. Harbola, J. Xiao, B. Y. Wang, *et al.*, Strain-induced room-temperature ferroelectricity in $SrTiO_3$ membranes, Nat. Commun. **11**, 3141 (2020).

[6] H. Wang, V. Harbola, Y.-J. Wu, P. A. van Aken, and J. Mannhart, Interface design beyond epitaxy: Oxide heterostructures comprising symmetry-forbidden interfaces, Adv. Mater. **36**, 2405065 (2024).

[7] M.-S. Kim, K. Lee, R. Ishikawa, K. Song, N. A. Shahed, K.-T. Eom, M. S. Rzchowski, E. Y. Tsymbal, N. Shibata, T. Mizoguchi, C.-B. Eom, and S.-Y. Choi, Charge disproportionation at twisted $SrTiO_3$ bilayer interface driven by local atomic registry, ACS Nano **19**, 39714 (2025).

[8] H. Sha, Y. Zhang, Y. Ma, W. Li, W. Yang, J. Cui, Q. Li, H. Huang, and R. Yu, Polar vortex hidden in twisted bilayers of paraelectric $SrTiO_3$, Nat. Commun. **15**, 10915 (2024).

[9] G. Sánchez-Santolino, V. Rouco, S. Puebla, H. Aramberri, V. Zamora, M. Cabero, F. A. Cuellar, C. Munuera, F. Mompean, M. Garcia-Hernandez, *et al.*, A 2D ferroelectric vortex pattern in twisted $BaTiO_3$ freestanding layers, Nature (London) **626**, 529 (2024).

[10] Y. Li, C. Xiang, F. M. Chiabrera, S. Yun, H. Zhang, D. J. Kelly, R. T. Dahm, C. K. R. Kirchert, T. E. L. Cozannet, F. Trier, *et al.*, Stacking and twisting of freestanding complex oxide thin films, Adv. Mater. **34**, 2203187 (2022).

[11] M. Schmidbauer, J. Maltitz, F. Stümpel, M. Hanke, C. Richter, J. Schwarzkopf, and J. Martin, Periodic lateral superlattice in bonded $SrTiO_3/SrTiO_3$ twisted perovskites, Appl. Phys. Lett. **126**, 101902 (2025).

[12] G. S. Rohrer, Grain boundary energy anisotropy: A review, J. Mater. Sci. **46**, 5881 (2011).

[13] D. Hull and D. J. Bacon, Dislocation arrays and crystal boundaries, in *Introduction to Dislocations*, 5th ed. (Butterworth-Heinemann, Oxford, 2011), Chap. 9, pp. 171–204.

[14] J. Eymery, F. Leroy, and F. Fournel, GIXRD of nanoscale strain patterning in wafer bonding, Nucl. Instrum. Methods Phys. Res. Sect. B **200**, 73 (2003).

[15] L. A. Hughes and K. van Benthem, Low-angle twist grain boundary in $SrTiO_3$ fabricated by spark plasma sintering techniques, J. Am. Ceram. Soc. **102**, 578 (2019).

[16] S. L. Sass, The study of the structure of grain boundaries using diffraction techniques, J. Appl. Cryst. **13**, 109 (1980).

[17] R. A. Wind, M. J. Murtagh, F. Mei, Y. Wang, M. A. Hines, and S. L. Sass, Fabrication of nanoperiodic surface structures by controlled etching of dislocations in bicrystals, Appl. Phys. Lett. **78**, 2205 (2001).

[18] F. Leroy, J. Eymery, P. Gentile, and F. Fournel, Controlled surface nanopatterning with buried dislocation arrays, Surf. Sci. **545**, 211 (2003).

[19] N. Pryds, D.-S. Park, T. S. Jespersen, and S. Yun, Twisted oxide membranes: A perspective, APL Mater. **12**, 010901 (2024).

[20] J. A. Alonso, I. Rasines, and J. L. Soubeyroux, Tristrontium dialuminum hexaoxide: An intricate superstructure of perovskite, Inorg. Chem. **29**, 4768 (1990).

[21] P. Su, H. Wen, Y. Zhang, C. Tan, X. Zhong, Y. Wu, H. Song, Y. Zhou, Y. Li, M. Liu, and J. Wang, Super-flexibility in freestanding single-crystal $SrRuO_3$ conductive oxide membranes, ACS Appl. Electron. Mater. **4**, 2987 (2022).

[22] S. Yun, T. E. le Cozannet, C. H. Christoffersen, E. Brand, T. S. Jespersen, and N. Pryds, Strain engineering: Perfecting freestanding perovskite oxide fabrication, Small **20**, 2310782 (2024).

[23] M. Kawasaki, K. Takahashi, T. Maeda, R. Tsuchiya, M. Shinohara, O. Ishiyama, T. Yonezawa, M. Yoshimoto, and H. Koinuma, Atomic control of the $SrTiO_3$ crystal surface, Science **266**, 1540 (1994).

[24] M. Schmidbauer, P. Schäfer, S. Besedin, D. Grigoriev, R. Köhler, and M. Hanke, A novel multi-detection technique for 3D reciprocal space mapping in grazing incidence x-ray diffraction, J. Synchrotron Rad. **15**, 549 (2008).

[25] D. Ingerle, Glancing incidence x-ray analysis, https://gixa.ati.tuwien.ac.at/tools/penetrationdepth.xhtml.

[26] M. Schmidbauer, A. Kwasniewski, and J. Schwarzkopf, High-precision absolute lattice parameter determination of $SrTiO_3$, $DyScO_3$ and $NdGaO_3$ single crystals, Acta Crystallogr. B **68**, 8 (2012).

[27] J. H. van der Merwe, On the stresses and energies associated with inter-crystalline boundaries, Proc. Phys. Soc. A **63**, 616 (1950).

[28] W. Bollmann, The individual dislocation: Geometrical basis, in *Crystal Defects and Crystalline Interfaces* (Springer, Berlin, 1970), pp. 41–50.

[29] S. L. Sass, T. Y. Tan, and R. W. Balluffi, The detection of the periodic structure of high-angle twist boundaries, Philos. Mag. **31**, 559 (1975).

[30] S. H. Sung, Y. M. Goh, H. Yoo, R. Engelke, H. Xie, K. Zhang, Z. Li, A. Ye, P. B. Deotare, E. B. Tadmor, *et al.*, Torsional periodic lattice distortions and diffraction of twisted 2D materials, Nat. Commun. **13**, 7826 (2022).

[31] M. Burian, B. F. Pedrini, N. Ortiz Hernandez, H. Ueda, C. A. F. Vaz, M. Caputo, M. Radovic, and U. Staub, Buried moiré supercells through $SrTiO_3$ nanolayer relaxation, Phys. Rev. Res. **3**, 013225 (2021).

[32] W. Sandholt, N. Gauquelin, J. Mangeri, E. Dollekamp, G. Panchal, T. Chennit, A. D. Backer, A. Annys, N. Vitaliti, A. R. Insinga, *et al.*, Designing dislocation-driven polar vortex networks in twisted perovskites, arXiv:2603.27272.

[33] Z. Zhang, W. Sigle, and W. Kurtz, HRTEM and EELS study of screw dislocation cores in $SrTiO_3$, Phys. Rev. B **69**, 144103 (2004).

[34] L. Fitting, S. Thiel, A. Schmehl, J. Mannhart, and D. A. Muller, Subtleties in ADF imaging and spatially resolved EELS: A case study of low-angle twist boundaries in $SrTiO_3$, Ultramicroscopy **106**, 1053 (2006).